DISTRIBUTION STATEMENT A. Approved for public release; distribution is unlimited.

Remote Sensing and Modeling of Coherent Structures in River and Estuarine Flows

Andrew T. Jessup
Applied Physics Laboratory
University of Washington
Seattle, WA 98195-5640
phone: (206) 685-2609 fax: (206) 543-6785 email: jessup@apl.washington.edu

Robert L. Street
Department of Civil and Environmental Engineering
Stanford University, Stanford, CA 94305-4020
phone: (650) 723-4969 fax: (650) 725-9720 e-mail: street@stanford.edu

Stephen G. Monismith
Department of Civil and Environmental Engineering
Stanford University, Stanford, CA 94305-4020
phone: (650) 723-4764 fax: (650) 723-3921 email: monismith@stanford.edu

Alexander R. Horner-Devine
Department of Civil and Environmental Engineering
University of Washington
Seattle, WA 98195-2700
Phone: (206) 685-3032 fax: (206) 685-9185 email: arhd@u.washington.edu

Award Numbers: N00014-05-1-0485 (MURI)

LONG-TERM GOALS

The long-term goals of this research are to combine state-of-the-art remote sensing and *in situ* measurements with advanced numerical modeling (a) to characterize coherent structures in river and estuarine flows and (b) to determine the extent to which their remotely sensed signatures can be used to initialize and guide predictive models.

OBJECTIVES

Coherent structures are generated by the interaction of the flow with bathymetric and coastline features. These coherent structures produce surface signatures that can be detected and quantified using remote sensing techniques. Furthermore, a number of relationships between coherent structures and flow characteristics have been suggested that have the potential to allow flow parameters (e.g. mean velocity, bottom roughness, shear, and turbidity) to be inferred from remote measurements. The objectives are to test the following four hypotheses:

1. Flow parameters can be inferred from remotely sensed signatures of coherent structures.
2. Numerical models can be constrained with these inferred parameters.

3. The effect of stratification on the strength of coherent structures can be used to detect the presence or absence of stratification and the location of the fresh/salt water interface.
4. Numerical and field experiments can be used together to predict, interpret, characterize, and understand coherent structures.

APPROACH

The key to this project is an interactive process that blends sophisticated remote sensing, in-situ measurements, and numerical simulation. Our approach is to conduct closely coupled field and numerical model experiments to test the hypotheses listed above. The plan includes two major field experiments with both *in situ* and remote sensing measurements – the first occurred in 2006 (Year 2) and the second occurred in 2009 (Year 5), and was planned using results from the pilot experiment which took place in September 2008. A preliminary experiment was conducted in 2005 (Year 1) to aid in the design of the major field efforts. The research involves four main areas - (1) *in situ* measurements, (2) remote sensing, (3) modeling, and (4) physics and classification of coherent structures. The *in situ* field measurements are used to characterize the overall flow field to investigate the generation of coherent structures at specific sites, and initially, to provide boundary inputs for the numerical models. The surface signatures of coherent structures in the same region are detected using remote sensing techniques and compared with the *in situ* and model results. Results from the *in situ* field observations, remote sensing, and numerical model runs will be synthesized into a classification scheme that includes all observed coherent structures. Predictive scaling relationships will be developed in order to generalize the results from this study to other systems. The result of this integrated approach will be a thorough investigation of the mechanisms and evolution of coherent structures in rivers and estuaries in order to link their surface expressions to subsurface flow features.

The project participants have been organized into teams identified by the main areas of interest listed above: Remote Sensing: A. Jessup, C. Chickadel (APL-UW), W. Plant and G. Farquharson (APL-UW); Modeling: R. Street and O. Fringer (Stanford); In situ Measurements: S. Monismith and D. Fong (Stanford); Physics and Classification: A. Horner-Devine and S. Talke (UW).

WORK COMPLETED IN FY10

The focus of this reporting period was:

- Analysis of data from the 2009 field experiment (Coherent Structures)
- Analysis of data from the 2006 field experiment (Estuary Dynamics)
- Modeling of 2006 field experiment (Estuary Dynamics)

RESULTS

This report will focus on the following areas (by lettered sections with lettered and numbered figures):

- A: 2009 Field Experiment Overview
- B: Thermal IR imaging of Coherent Structures (barge and airborne) (UW, APL)
- C: Physics and Classification of Coherent Structures – lab expt. (UW, Civil and Env. Eng.)
- D: In Situ Measurements of Estuary Dynamics and Coherent Structures (Stanford)
- E: Numerical Modeling of Estuary Dynamics (Stanford)
- F: Microwave Remote Sensing (UW, APL)

A: 2009 Field Experiment Overview

The final major field experiment of the project was conducted from 8-25 Sep 2009 on the Snohomish River in Everett, WA. The UW research barge R/V Henderson was used to acquire infrared imagery and near surface turbulence measurements. The left photograph in Figure A1 shows the instrument boom (raised position) attached to the bow of the Henderson. The front of the boom has a sub-surface frame with an array of velocity sensors and the tower with an infrared camera. The Henderson was equipped with movable pilings, or spuds, which provided rapid mobility that allowed us to make measurements routinely on both flood and ebb tides. The spuds also provided exceptional stability for the turbulence measurements. The right photograph in Figure A1 shows the Helikite platform used to provide large area infrared imagery.

Figure A1. (left) Photograph of UW research barge R/V Henderson showing instrument boom used for infrared imagery and subsurface turbulence measurements. (right) Photograph of Helikite used for large field-of-view infrared imagery.

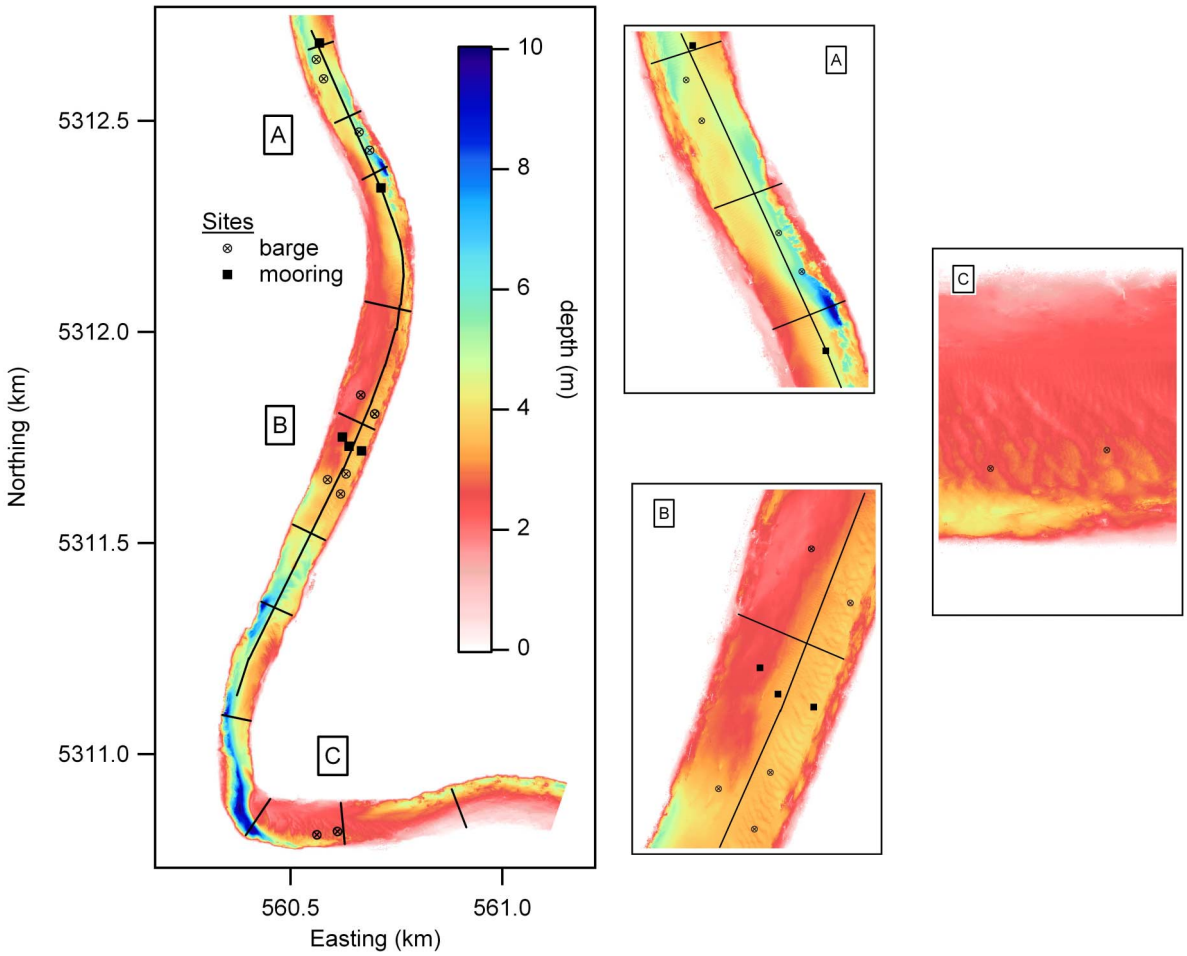

Figure A2. 2009 Study Region. (left) Overview and (right) Sites A-C in detail. The line along the channel marks the path of REMUS while cross channel lines indicate ADCP/CTD transect paths. The two moorings at site A are A1 (north) and A2 (south). The three moorings at site B are labeled B1, B2, and B3 from west to east. No moorings were at site C.

The measurements were made at three sites within a 2.5 km stretch of the river located approximately 15 km upstream from the mouth. The distance upstream was chosen in order to minimize the influence of stratification. The specific stretch of river was chosen because of the proximity of a variety of bathymetric features of interest. Figure A2 shows on overview of the bathymetry of the study area details of the individual sites designated as A-C. The figure shows the location of the barge at each site as well as the moorings, which were located at sites A and B only.

B: Thermal IR imaging

Nested-scale thermal infrared (IR) imagery was gathered during a 2009 field experiment on the Snohomish River from a suite of imaging platforms (spanning millimeters to tens of meters). We continue our investigation of this data by focusing on the spatial and temporal development of observable surface coherent structures and how they relate to the underlying flow conditions (esp. depth and bottom roughness). During FY2010 our research has included:

1. Refinement and validation of our 2D Particle Image Velocimetry (PIV) algorithm for IR video, calculation of surface flow statistics from 2D PIV including TKE and TKE dissipation rates with comparison against in situ data, and

2. Estimation of large-scale river velocity, *O*(10-100 m), from the LTAIRS (Lighter-Than-Air InfraRed System) deployments.

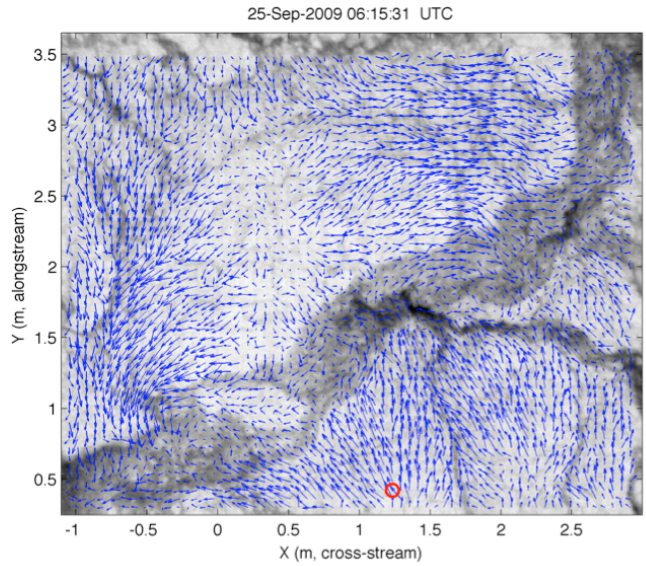

Figure B1. Snapshot of residual PIV estimated flow vectors associated with the simultaneous IR image of and erupting boil (the large bright - warm - feature). A red circle indicated the position of a collocated ADV sampling at 2cm below the water's surface.

Small-scale surface velocity

Particle image velocimetry analysis was performed on IR image data collected at a frequency of 5 Hz (sub-sampled from 20 Hz data) from a tower-mounted, cooled IR imager on board the *R/V Henderson*. The average pixel resolution over the imaged field is 7.5 mm, providing resolution of fine-scale temperature features. The PIV technique we have developed measures horizontal velocity by tracking shifts in coherent temperature patterns across sequences of infrared images. The technique used here is based on phase correlation, as opposed cross-correlation, to better define image feature motion in the presence of large-scale background variation [Wernet, 2005]. We implement a multigrid algorithm so that coarse estimates are used for quantifying finer scale flow features in a highly turbulent flow. An example residual 2D flow field (spatial mean removed) is shown overlain on an IR image of an erupting boil in Figure B1, and demonstrates the complex flow patterns observed.

IR PIV results were validated against near surface measurements from a collocated Acoustic Doppler Velocimeter (ADV). The mean along-stream flow and cross-stream flow ($\langle v \rangle$ and $\langle u \rangle$) and its temporal perturbation (v' and u') estimated with the IR-PIV technique agree well with the results of in situ velocimeter measurements (Figure B2a and B2b). Similarly, power spectra (Figure B3c) of cross-stream and along-stream velocity derived from PIV and from the in-situ velocimeter agree quite well, particularly for larger scale motions with a frequency of $f < 1$ Hz. Above 2 Hz, the spectra begin leveling out, indicating that a noise floor is approached. The spectra from both instruments exhibit an $f^{-5/3}$ decay, consistent with a classic Kolmogorov turbulent cascade.

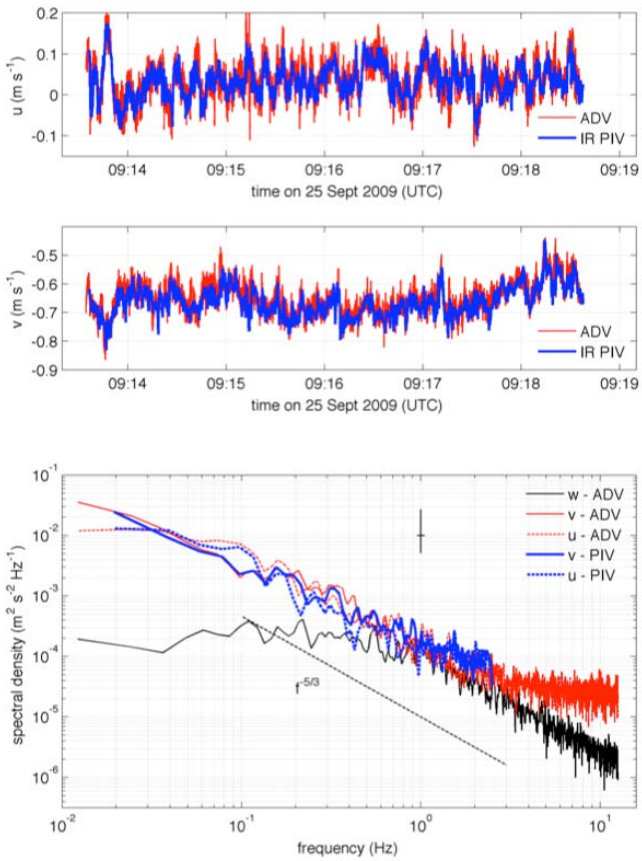

Figure B2. PIV and ADV comparisons of the cross-stream (top panel) and alongstream (middle panel) surface river velocities for a 5-minute time series. Both measurements show good agreement. Spectra of the individual components (lower panel) show similar agreement, including an $f^{-5/3}$ decay typical of a turbulent energy cascade.

A systematic statistical comparison between the ADV and PIV measurements were made over during several hours on an ebb tide (from high to low water) as flow speeds increased from slack to ~0.7m/s, as is shown in Figure B3. Three-minute averaged along-stream velocities ($<v>$) from this ebb tide are highly correlated with ADV measurements ($r^2 = 0.999$; Figure B3). Cross-stream mean velocities ($<u>$) are similarly correlated ($r^2 = 0.94$), with PIV estimates 2% larger than ADV measurements. The well-resolved turbulent velocity signal allows for calculation of higher order statistics such as TKE and ε. Horizontal portions of the TKE ($<v'^2>/2 + <u'^2>/2$) show good correlation between both estimates ($r^2 = 0.85$). Turbulent energy dissipation (ε) estimates, found by fitting an $f^{-5/3}$ slope to the inertial subrange, shows good agreement between both methods ($r^2 = 0.59$). We attribute the small difference in TKE and ε between methods to instrument noise, the spatial resolution in the PIV, and possible flow bias in the in situ measurement frame.

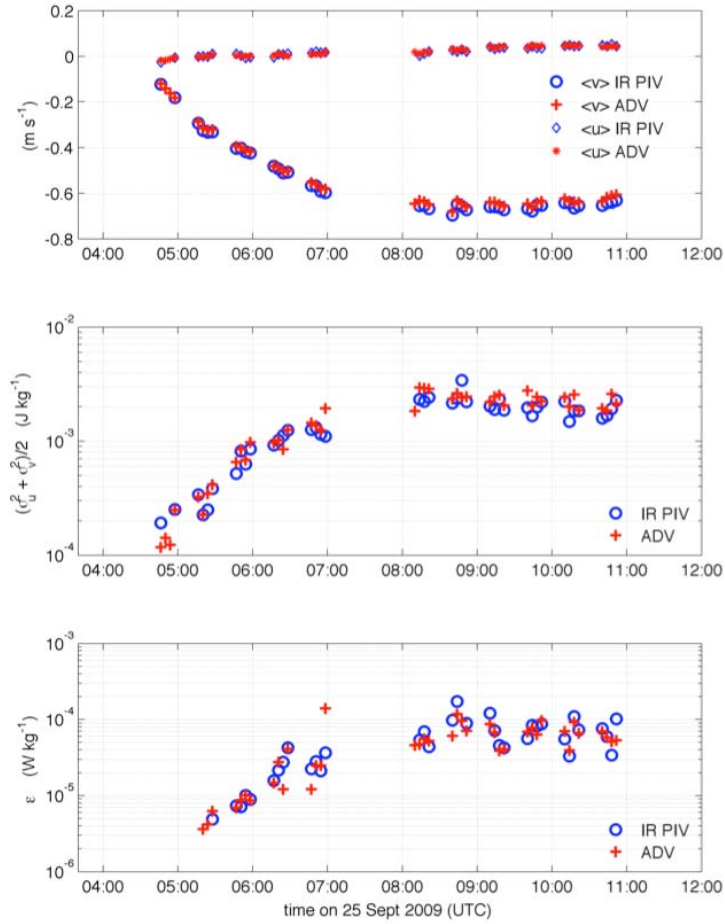

Figure B3. Time series comparisons of three-minute statistics over an ebb tide, including (top panel) mean alongstream (<v>) and cross-stream velocities (<u>), (middle panel) computed horizontal turbulent kinetic energy, and (lower panel) computed turbulent energy dissipation (ε).

The presence of an $f^{-5/3}$ slope in velocity spectra at the water surface is a surprising result, since *Kolmogorov* [1941] specifically assumes that an inertial cascade requires isotropic conditions. Because vertical velocity fluctuations are suppressed by the surface (kinematic) boundary condition, the expected surface flow might be expected to be highly anisotropic, without a turbulent cascade. However, other studies have also found a -5/3 slope at the surface [e.g. *Tamburrino and Gulliver*, 1994] and used the inertial subrange method to estimate dissipation, noting however that its interpretation is somewhat controversial [*Brumley and Jirka*, 1987].

Large-scale river flow

A now routine aerial platform, the Lighter-Than-Air InfraRed System (LTAIRS) was deployed to collect river width (100m) IR imagery of moving surface temperature patterns that can be used to investigate surface boil disruption and estimate surface flow from PIV. Useful results from PIV require input time series images that are rectified to real world coordinates, however high frequency motion not measured by the attitude sensors in the LTAIRS needed to be corrected by frame-to-frame image registration. This was accomplished by automated post-processing to match stationary ground features and targets, including the riverbank and the moored barge. An example 1-minute averaged PIV velocity field imaged from the LTAIRS is shown in Figure B4, and it demonstration the effectiveness of PIV on slowly moving airborne imagery with remarkable results.

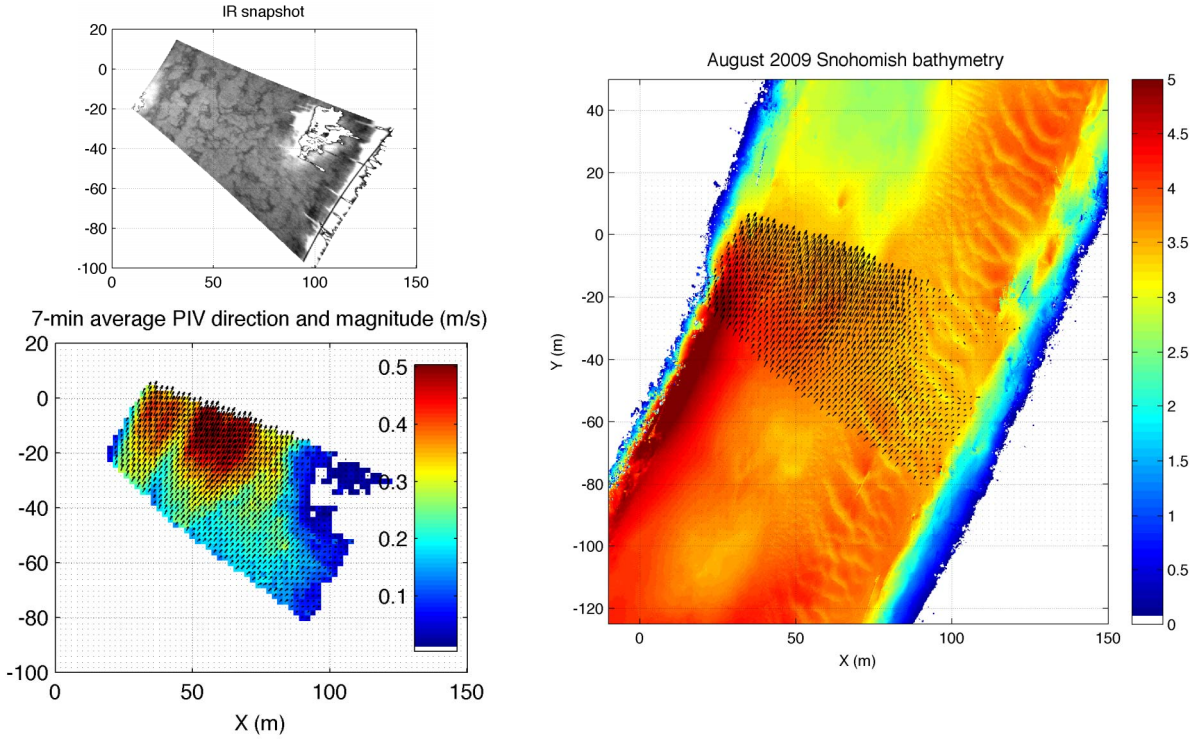

Figure B4. (top left) A sample IR snapshot from the Helikite platform rectified to the river's surface is shown for reference. (lower left) A calculated one-minute mean PIV velocity field estimated from LTAIRS image data recorded from the lower Snohomish River. Data centered at x = 100m, y = -40m is removed where the APL research barge is imaged. Note the near regular pattern of alternating high and low flow regions parallel to the mean river flow indicating cellular river circulation in response to bathymetry. (right) Shallow water multibeam of the Snohomish River in the IR field of view.

Even at relatively slow river flow (20cm/s) the PIV velocity field reveals both longitudinal and lateral variability, specifically alternating slow and fast flow lanes in the river. These velocity patterns could be related to secondary circulation cells in response to bathymetry at this site [*Nezu et al*., 1993], which prompts at least two possibilities for estimating river bathymetry variations from airborne IR video time series. First, the alternating surface cellular flow pattern has been shown to have a predictable lateral structure in laboratory rivers with wide aspect ratio (width/depth > 7-10), such that lateral spacing between upwelling locations (where boils are present) is approximately twice the river depth [*Tamburrino and Gulliver*, 2007]. Cellular spacing could be estimated from PIV velocity fields, or directly from boil streets imaged in IR snapshots. The second depth estimation method would be to use the surface flow field input into the mass conservation equation and integrate to obtain the depth variability. Absolute depths estimated by this technique will require a known starting depth, and a logical choice is the bank, which is approximately zero.

C: Physics and Classification of Coherent Structures

During the 2009 field experiment, in situ velocity measurements were made within the IR field of view with three primary objectives:

1. to determine the subsurface velocity structure of boils observed in the IR imaging
2. to compare subsurface turbulence statistics with those derived from the IR fields

3. investigate the distortion of turbulent eddies resulting from the free-surface

Instruments were mounted on a rigid frame, which was mounted to the A-frame on the R/V Henderson. During sampling periods the R/V Henderson was rotated so that the A-frame and instrument frame was oriented into the flow (up-river or down-river on ebb and flood, respectively) and the flow sampled with the instruments was far from any possible contamination from the vessel. The instrument array consisted of four vertically spaced Acoustic Doppler Velocimeters (ADVs) positioned 1.5m, 0.7m, 0.4m and 0.2m from the water surface and two laterally spaced ADVs located 1.1m and 0.6m from the center. Two Nortek Aquadopp Acoustic Doppler Profilers (ADPs) were mounted to the frame; one mounted 1m below the water surface in an up-looking configuration and the other mounted 0.3m below the water surface in a side-looking configuration. Finally, a 1200kHz RDI ADCP was mounted on the A-frame 2.5m behind the ADV/ADP frame.

The most significant challenge to making turbulence measurements using ADVs on a floating platform such as the R/V Henderson is ensuring that they are not contaminated by vessel movement (pitch, roll, or vibration) or vibration of the frame relative to the vessel. Vessel movement was operationally eliminated as a result of the new 5000lb spuds that were installed fore and aft on the Henderson. Although boat wakes during daylight hours still resulted in some platform movement, very little movement occurred during our sampling periods, which were at night.

a) b)

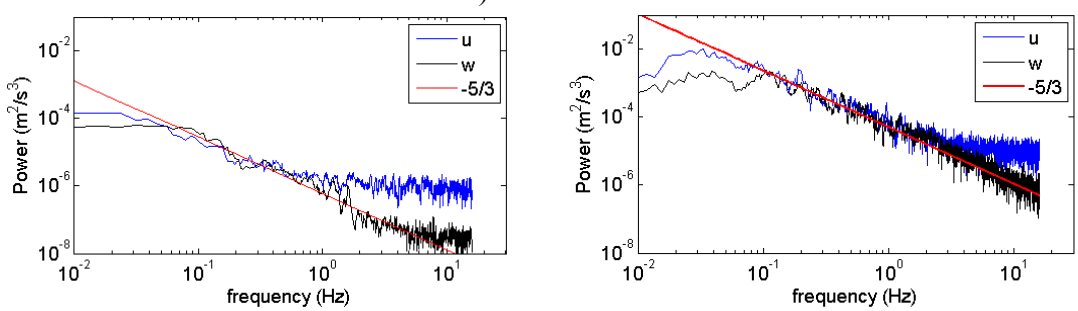

Figure C1: Power spectra for low (a) and high (b) velocity periods. Both spectra show very clear -5/3 slopes corresponding to the inertial subrange.

We were able to resolve turbulent motions for very slow, low energy flows (u = 0.16m/s, tke dissipation = 6 x 10^{-8} W/kg) and faster, more energetic flows (u=0.6m/s tke dissipation = 1.5 x 10^{-5} W/kg). Power spectra for these two cases are shown in Figure C1. Both cases display very clear -5/3 slopes, indicating that we resolve the inertial subrange over more than two orders of magnitude, even in very low energy conditions.

Conditional sampling and the vertical structure of boils. Boils are visible on the water surface as anomalously warm regions in the IR images due to disruption of the cool skin layer. Since our in situ instrumentation (ADV, ADP) is located within the IR field of view, we use the IR field to conditionally sample the data from the subsurface instrumentation.

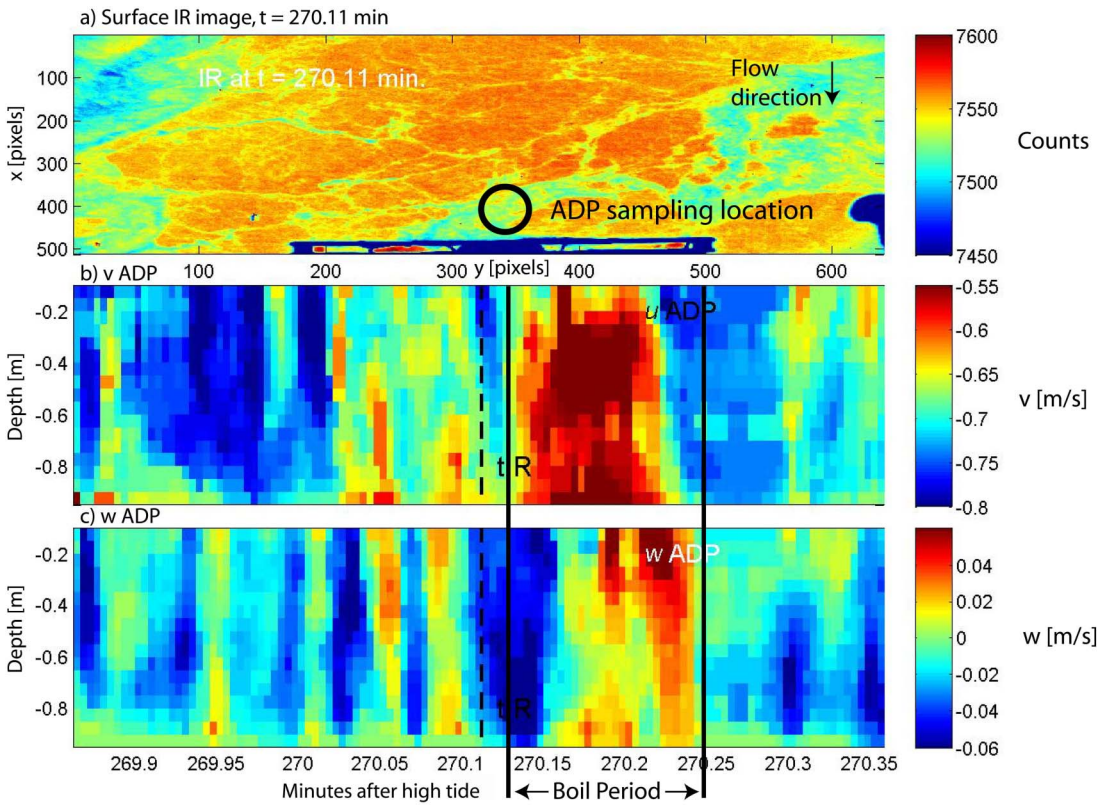

Figure C2: a) Uncalibrated IR image showing a passing boil (warm colors) on the water surface. The typical temperature range is less than 0.7°K. Profiles of b) streamwise horizontal and c) vertical velocity measured with the ADP at the location indicated in a). The dashed line corresponds to the time of the IR image.

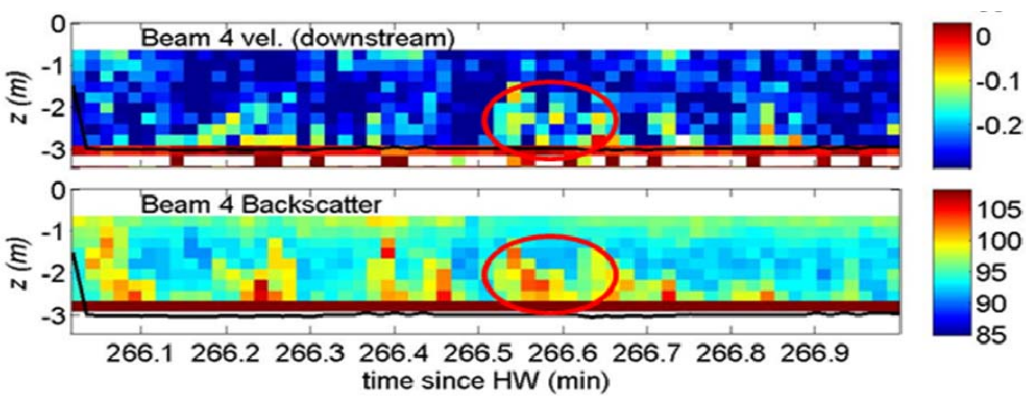

Figure C3: Beam velocity and acoustic backscatter measured with the down-looking ADCP showing the vertical extent of the boil signal. These measurements are three minutes before the boil signal shown in Figures C2 and C4.

This allows us to differentiate between the boil and non-boil periods and determine the structure and turbulent statistics of the boils. A good example of this is shown in Figure C2. An uncalibrated IR image is shown in panel a) corresponding to 270.11 min after high tide. Flow is toward the bottom of the image and a large boil is about to cross over the ADP sampling volume, which is shown as a black circle in the image. The horizontal and vertical velocity profiles measured with the ADP clearly show that the boil consists of fluid that is slower (~10cm/s) than the background flow and is marked by

strong downwelling (~5cm/s) at its leading edge and upwelling (~5cm/s) in the middle. The vertical structure extends at least 1 m below the surface in these profiles; however, beam velocity and acoustic backscatter measured with the down-looking ADCP at approximately the same time show that the boil signal extends all the way to the river bottom (Figure C3).

Horizontal surface structure of boils. The surface velocity field corresponding to the boils was determined by C. Chickadel using the PIV technique described earlier. Based on the derived velocity field, instantaneous streamlines can be computed that aid in visualizing the horizontal flow structure of boils. Figure C4 shows four snapshots of boil structure corresponding to the same period as is shown in Figure C2.

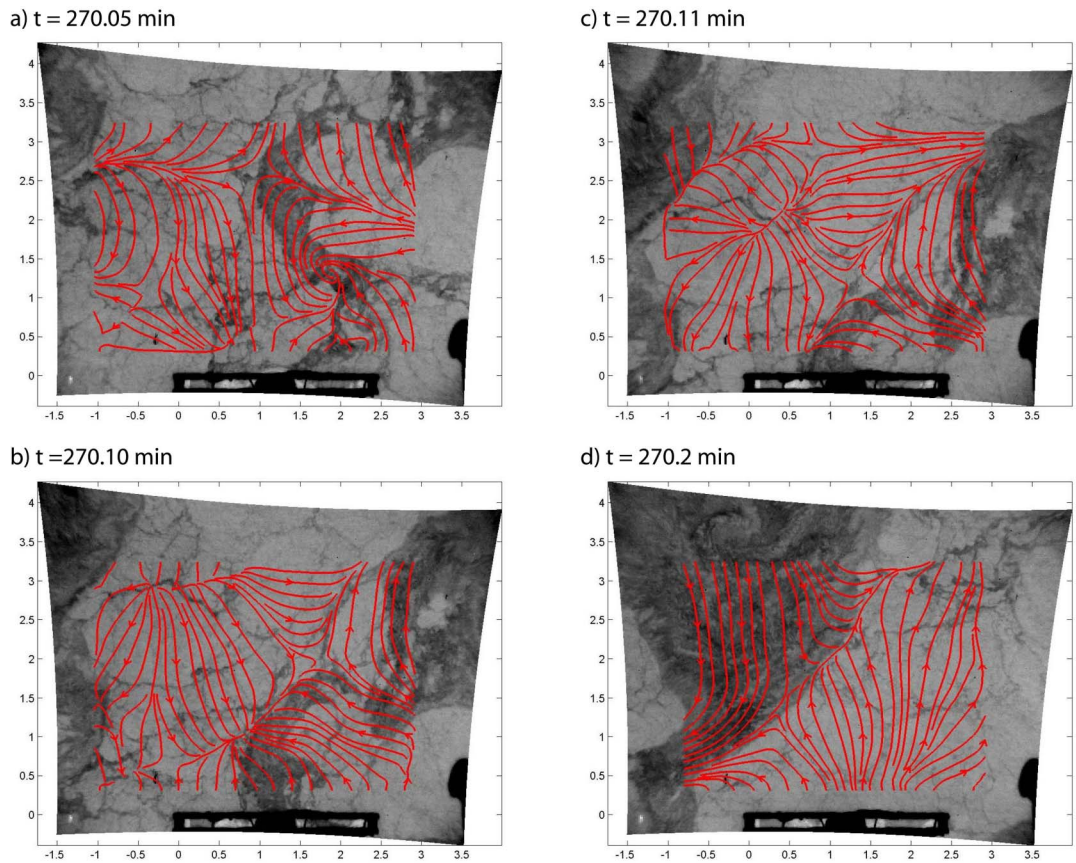

Figure C4: Surface IR field (greyscale) and overlaid instantaneous streamlines (red) during the passage of the boil whose vertical structure is shown in Figure C2b and C2c.

These snapshots and subsequent statistical analysis (not shown) show that vorticity is concentrated in the fluid on the edges of the boils and between boils and is lower within the boils themselves (Figure C3a). This is somewhat counter to a popular description of a coherent structure as "a connected, large-scale turbulent fluid mass with phase-correlated vorticity over its spatial extent" (Hussain, 1983). The surface velocity fields also resolve strong convergence along the edges of the boils and divergence in the center of the boils (Figures C3b, c, and d), consistent with the vertical structure shown in Figure C2. In general, the surface flow is dominated by boil structures, which are significantly slower than the ambient flow and act as obstacles to that flow; the boils divert faster surface flow around them, causing strong lateral shear and vorticity.

Near surface turbulent structure. Using the velocity measured with the near-surface array of ADVs we determined turbulent statistics over a 6.5 hour period of the ebb tide starting at high slack (Figure C4). The vertical component (w'^2) of turbulent kinetic energy (tke) and the tke dissipation rate (ε)increased by more than two orders of magnitude, from 1e-5 m^2/s^2 to 2e-3 m^2/s^2 and from 1e-7 W/kg to 1e-4 W/kg, respectively. Both w'^2 and ε show a strong surface effect, with w'^2 decreasing by an order of magnitude close to the surface (2 cm) relative to the middle of the water column (150 cm). However, the power spectra still show a clear inertial subrange marked by a -5/3 slope, as observed in isotropic turbulence. The lowest frequency (longest wavelength) in the inertial subrange is observed to increase (decrease) closer to the surface. By comparing the tke in the inertial subrange we were able to show that the turbulence still appears to be isotropic at smaller scales close to the surface (not shown).

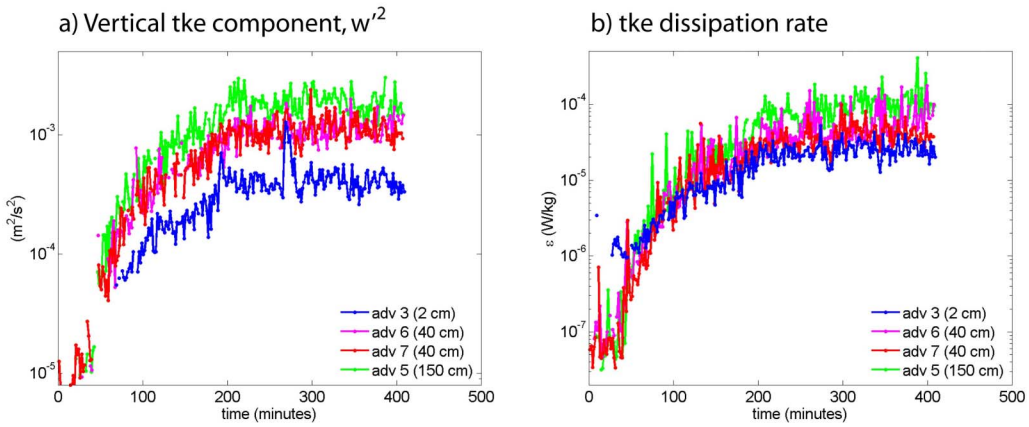

Figure C5: a) Vertical tke component (w'^2) and b) tke dissipation rate (ε) measured at 3 depths (2 cm, 40 cm and 150 cm below the water surface) during ebb tide starting at high slack. The maximum depth – averaged velocity is 0.6 m/s and occurs after 250 minutes.

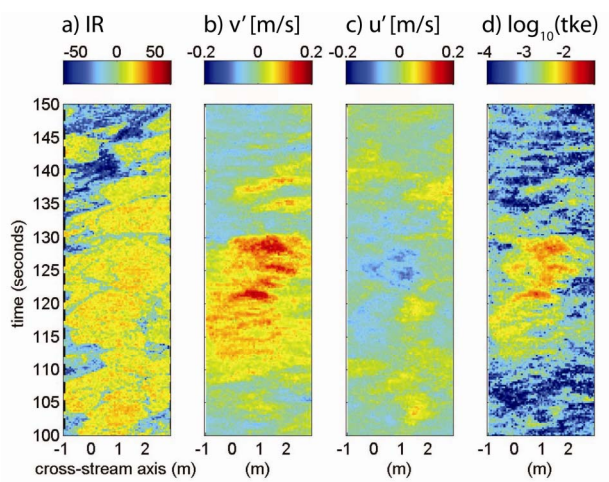

Figure C6: Time-stacks of a) de-trended IR, b) de-trended along stream velocity v', c) de-trended cross-stream velocity u', and d) horizontal TKE as a function of cross-stream direction. The data in these panels are taken from the IR images and the IR-derived surface velocity field, sampled along a line normal to the flow direction.

Turbulent structure of boils. We generate a time-stack of IR temperature anomaly (Figure C6a) for comparison with the derived turbulent fields (Figures C6b, c, and d). This analysis shows that the boils

are relatively slower (positive v') than the background flow (Figure C6b). It also suggests that turbulent kinetic energy is elevated in boils (Figure C6d). A similar comparison of the IR field with vertical vorticity, swirl and horizontal divergence confirms that vorticity and swirl are high is the fluid surrounding the boils and divergence is high within the boil (not shown).

To compute turbulent statistics, we aggregate over all within-boil or non-boil periods exceeding 2.5s (65 samples with the ADV). The turbulent kinetic energy is approximately twice as high in the boils as it is in the ambient fluid (Figure C7a). Power spectra from boil and non-boil periods sampled with ADV3 (2 cm below the water surface) are shown in Figure C7c. The spectra are not as clean as those shown in Figure C1 because the sample periods are within an individual boil or between boils and are consequently quite short. Nonetheless, both show -5/3 regions indicating that we are capturing the inertial subrange. The energy in the boil spectra is significantly higher than the non-boil spectra. Dissipation of tke is computed from boil and non-boil spectra for all continuous periods longer than the minimum sampling duration and bin averaged to generate a timeseries of dissipation over 3.5 hrs of the ebb sampling period (Figure C7d). Spectra that deviate significantly from the expected -5/3 slope are excluded from the analysis. The error bars are relatively large due to the short sampling periods. However, we observe that the dissipation rate is 2-3 times larger in the boils than in the ambient fluid. A popular model for estimating air-water gas transfer assumes that transfer depends strongly on the ratio of dissipation rate within boils to that in the ambient fluid (Moog and Jirka, 1999); however there are few estimates of this ratio and they are limited to flume experiments. We anticipate that these data will provide new insights into the processes of air-water gas exchange.

Finally, estimates of the tke budget through the water column (not shown) indicate that production exceeds dissipation near the bottom, while dissipation exceeds production near surface; the difference is the result of vertical turbulent transport. Since the boils are marked by elevated tke, they represent a likely and important mechanism for this transport. In Figure C7b we estimate the vertical turbulent transport observed near the water surface during boil and non-boil periods. There is a net upward transport in boils (8.6e-5 m^2/s^3) and downward transport in the ambient fluid (-5.8e-5 m^2/s^3). The difference (2.7e-5 m^2/s^3) is a net upward transport, which must be balanced by the dissipation at the surface in the absence of local production. As shown in Figure C5b dissipation at the surface is approximately 3e-5 m^2/s^3, consistent with the net transport.

Relationship between surface turbulence and water-column turbulence. Water column estimates of dissipation rate and tke were made using data from the downlookind ADCP and compare well with the near-surface and surface estimates from the ADV and IR respectively. Figure C8 shows water column profiles of normalized dissipation and tke, which display a consistent variation with depth. The profile are normalized by the shear velocity u_* and the depth, H. The consistency of the depth profile, which has been observed previously (Stacey and Monismith, 1999; Nezu and Nakagawa, 1993) suggests that measurements dissipation and tke could be used to solve for the two normalizing parameters, u_* and H. Furthermore, since the IR-derived estimates of dissipation and tke agree well with the near-surface measurements, it may be possible to use remotely sensed data to determine u_* and H, which are valuable inputs for driving a numerical model.

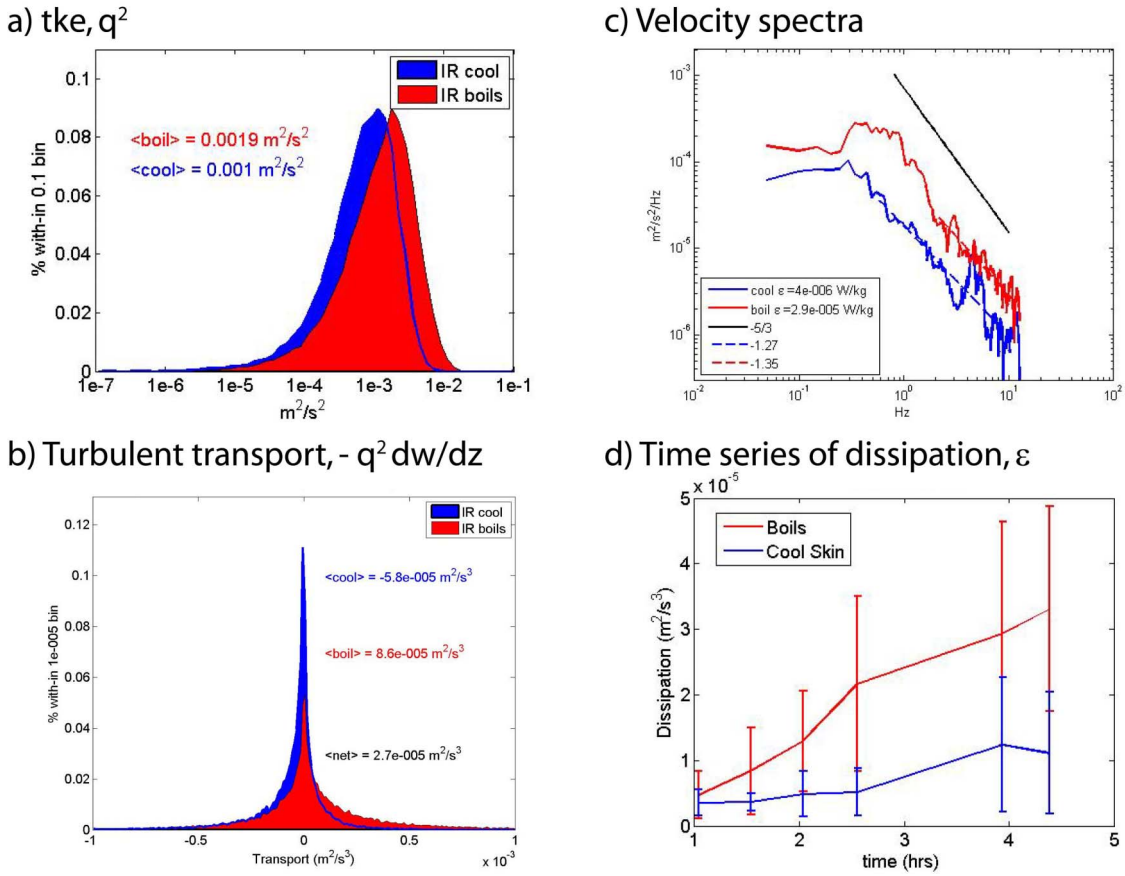

Figure C7: Comparison of turbulent statistics between within-boil (red: warm IR anomaly) and non-boil (blue: cool IR anomaly) regions. a) PDF of turbulent kinetic energy, b) PDF of turbulent transport, c) power spectra, and d) timeseries of turbulent kinetic energy dissipation rate, ε.

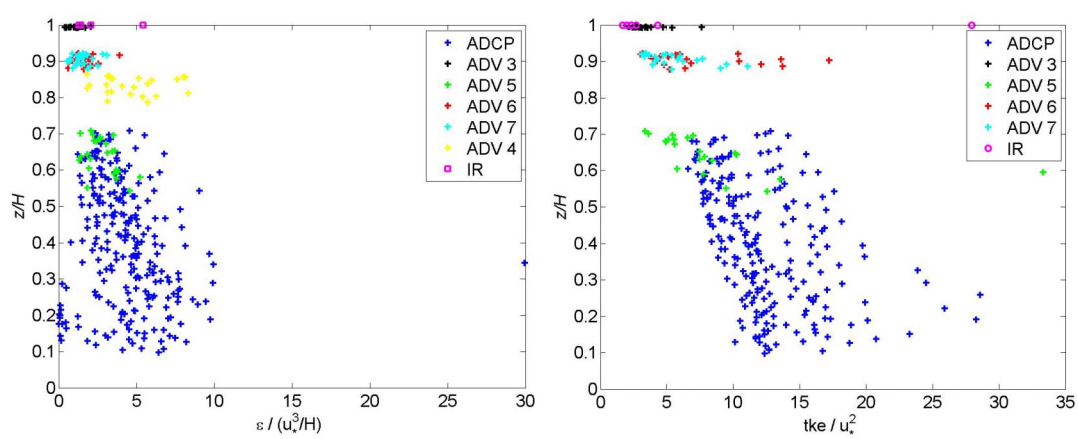

Figure C8: Normalized profiles of dissipation and tke derived from a downlooking ADCP, a vertical array of near-surface ADVs and surface IR velocity measurements.

D: *In-situ* field measurements

During FY2010 our efforts have been focused on further analysis of the data obtained in July 2006 and September 2008 and 2009. The work completed on the 2006 data has been incorporated into one submitted manuscript, presentations at several conferences, and two papers in preparation. The work completed on the 2008 and 2009 measurements has also been presented at several conferences and is the subject of an additional manuscript in preparation.

Further analysis of July 2006 data

The active areas of research utilizing the 2006 dataset include a detailed analysis of both the intratidal variability and the subtidal dynamics in the Snohomish River Estuary (SRE). On the tidal time scale we focus on the evolution of stratification vertical mixing, and longitudinal dispersion as well as frontal dynamics. This analysis provides good insight to the dynamics in similar strongly forced, strongly stratified estuarine systems which are prevalent yet less well studied than partially mixed systems. To further understand the dynamics unique to shallow, macrotidal estuarine systems and systems with large intertidal regions or regions with large tidal amplitude to depth ratios we examined the subtidal variability of the SRE and tried to compare the observed dynamics to those common in mesotidal and microtidal systems.

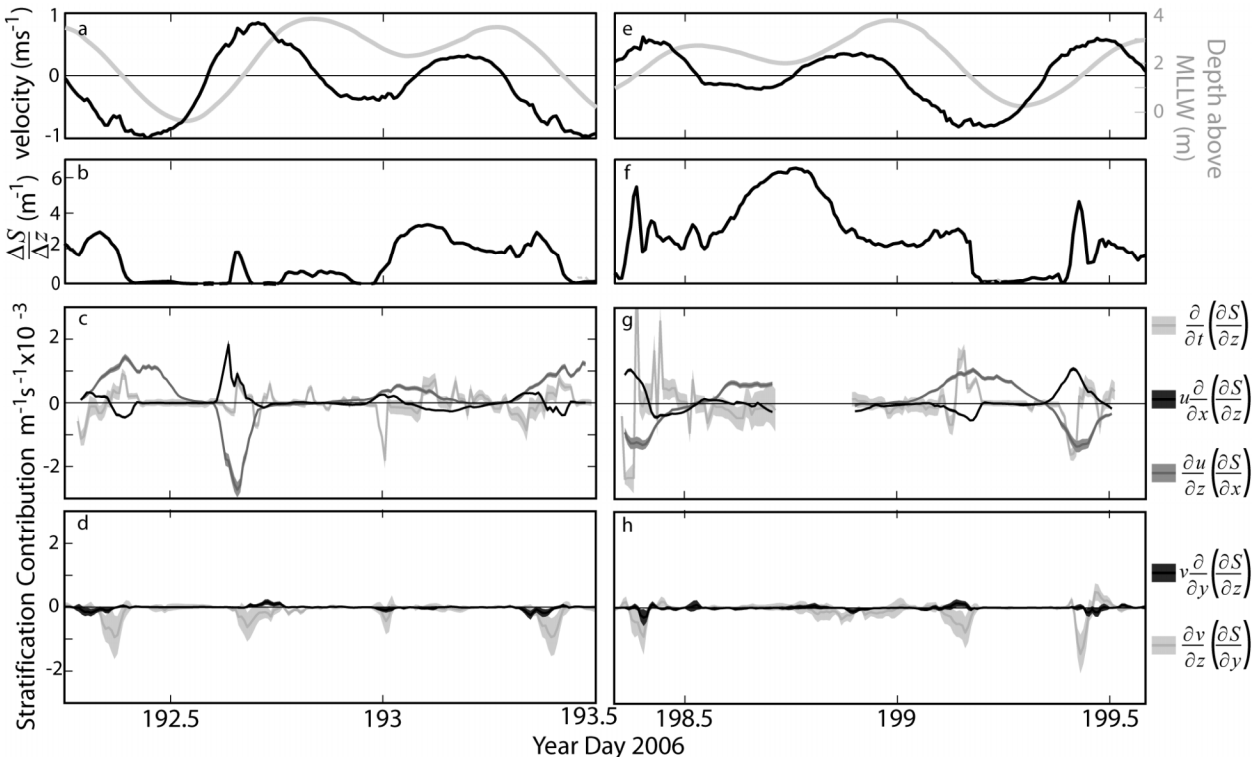

Figure D1. Stratification Evolution at mooring M3B The panels from top to bottom display mean velocity and water level (a, e), top bottom stratification (b, f), and the depth-average of terms contributing to the evolution of stratification (c, g and d, h) for a spring tide (left panels) and neap tide (right panels). The terms displayed in the last two rows include the unsteady evolution of stratification, along stream advection of stratification, along stream straining, lateral advection of stratification, and lateral straining respectively.

Intratidal dynamics
A paper currently under review examines the role of straining and advection in the intratidal evolution of stratification, vertical mixing, and longitudinal dispersion in the SRE. Due to the salt-wedge nature of the system, both along-stream advection and concomitant straining of the density field dominate temporal and spatial variations in stratification (*Figure D1*). The dynamics of the straining and advection vary substantially on both a tidal time scale and a fortnightly time scale leading to strong temporal variability in stratification, vertical mixing, and longitudinal dispersion that differs in important ways from observations in partially-mixed estuaries. In particular, flood tide advection is counteracted by straining and vertical mixing such that stratification, shear, and longitudinal dispersion are minimal. In contrast, ebb-tide straining and advection enhance vertical stratification and vertical shear which enhances longitudinal dispersion and leads to strong ebb-tide interfacial mixing. Based on these observations it is clear that similar tidal scale variability in stratification and mixing must also play an important role in other strongly forced, strongly stratified estuarine systems where common approximations such as a constant horizontal salinity gradient, $\partial S/\partial x$, or a small amplitude, $\eta/h<<1$ do not hold.

Frontogenesis
Following on the theme of important intratidal variability in the SRE, particularly variations in stratification and mixing, we finished our investigation of the dynamics of a repetitive frontal feature. Complex bathymetry in the SRE leads to trapping of mid-density water over intertidal mudflats which later converges with dense water in the main channel forming a sharp front. The frontal density interface is maintained via convergent transverse circulations driven by both lateral baroclinic and centrifugal forcing. The frontal presence and propagation lead to spatial and temporal variations in stratification and vertical mixing. Importantly, the front leads to enhanced stratification and suppressed vertical mixing at the end of the large flood tide. Despite these local effects, this front does not significantly alter longitudinal dispersion. This frontogenesis mechanism fits within the broader context of bathymetrically driven frontogenesis mechanisms in which varying bathymetry drives lateral convergence and baroclinic forcing and we expect it to occur in other systems, potentially even contributing to longitudinal dispersion in estuaries with larger trapping regions. This investigation benefited from the entire suite of COHSTREX measurements including numerical simulations, RiverRad, TIR imagery, REMUS and our other in-situ instruments. The results of this investigation have been included in a manuscript to be submitted shortly with several of the other COHSTREX investigators.

Subtidal dynamics
The most recent area of research on the 2006 data has been investigation of subtidal dynamics. Previous work emphasized the strong intratidal variability in this system and the dominant forcing mechanism of the barotropic tides. Most estuarine systems exhibit residual (subtidal) circulation driven by the baroclinic forcing, i.e. upstream at depth and downstream at the surface which is considered a critical factor in residual transport processes. Residual circulation is difficult to interpret however in a shallow, macrotidal system where the tidal amplitude is comparable to the mean depth. Profiles of residual circulation and residual density structure are shown in *Figure D2* below. We have been working on several approaches including data manipulation and analytical work to try to interpret the observed residual circulation structure.

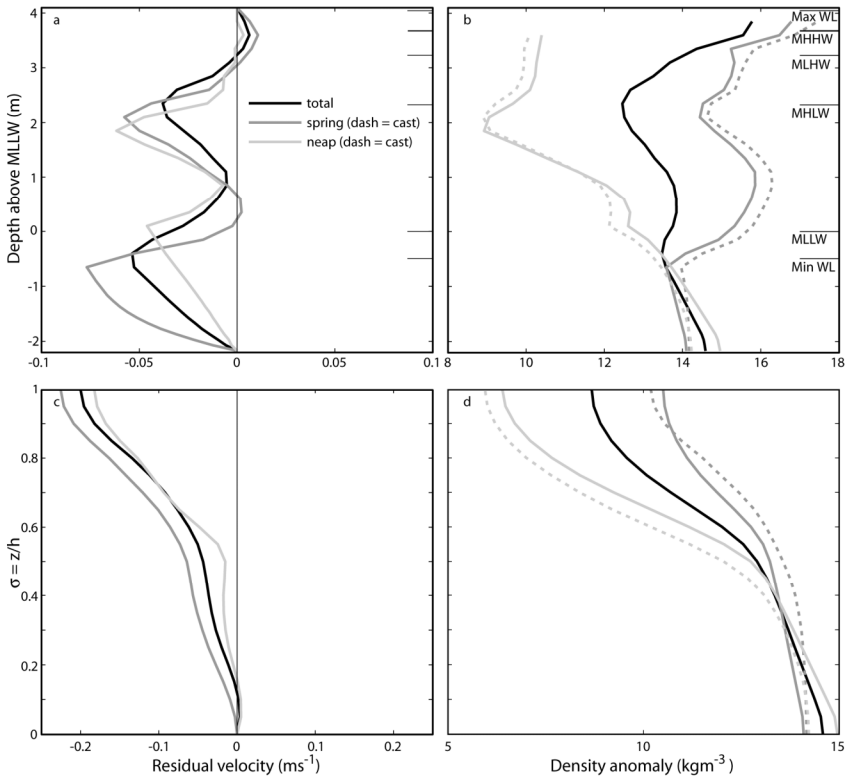

Figure D2. Residual circulation This figure displays residual (tidally averaged) circulation (left panels) and density profiles (right panels) in traditional z coordinates (upper panels) and depth normalized, σ, coordinates (lower panels). The totals are presented for a full 14 day spring/neap cycle (black lines) as well as for individual spring (grey) and neap (light grey) cycles. The density profiles shown in dotted lines are computed from CTD casts in the channel center while the solid lines represent interpolations of the density from near surface, near bed, and mid-water column moored CTDs. Positive velocity is in the flood tide direction, or upriver.

The residual circulation does not exhibit the traditional estuarine structure (*Figure D2a)*, rather there is out-estuary flow at the bed and a couple peaks mid water column. If we convert our coordinate system to a normalized depth coordinate system, $\sigma = z/D$ where D is the temporally varying total water depth, the residual circulation profile cleans up substantially (*Figure D2c*) and in fact resembles more of a traditional estuarine circulation. Similarly the density profiles exhibit the more expected residual profiles as opposed to the z coordinate system where they actually exhibit unstable residual profiles.

The normalized depth coordinate system is a very useful system to work in with this type of estuary because it eliminates large amounts of missing data when the water level is beneath high water. We performed an empirical orthogonal function (EOF) analysis on the data in σ coordinates and found that the first two modes represented over 99% of the variability in the data and correlated significantly with the depth averaged velocity and the vertical stratification respectively suggesting that EOF1 represents a barotropic mode while EOF2 represents a baroclinic mode. Recreating our data from the first two EOFs and returning to z coordinates allowed us to better interpret the z profiles. The left panel of *Figure D3* shows that the strange z profiles are created via a combination of a traditional baroclinic circulation as well as a strong tidal residual circulation.

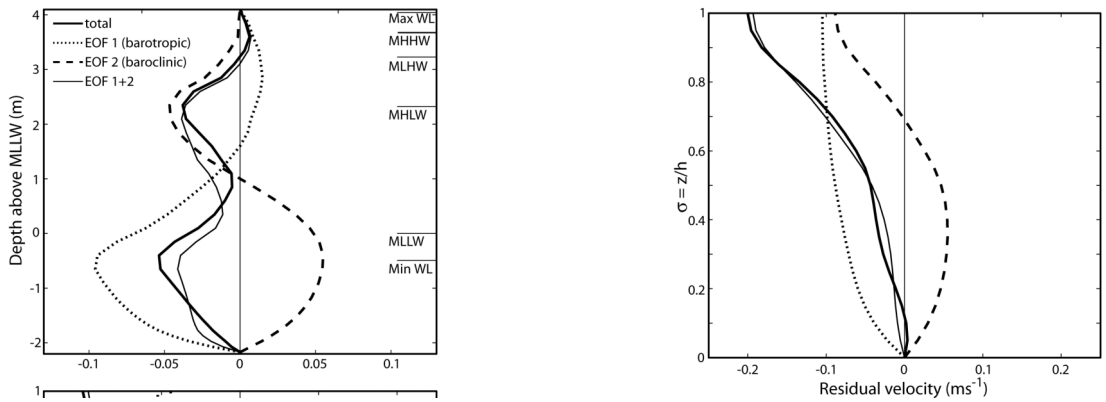

Figure D3. EOF components of the residual circulation. The first (dotted line) and second (dashed line) residual EOFs and their sum (thin line) are presented along with the total residual (thick line) over a 14 day spring/neap cycle in both z coordinates (left panel) and σ coordinates (right panel).

This work has continued by examining analytical solutions to the tidally averaged momentum equations in σ coordinates and comparing this to traditional estuarine theory. Additionally we have examined the tidally varying momentum equations in detail and hypothesized that like many other estuarine systems, this residual is actually driven by intermittent pulses of two layer circulation created by straining, intratidal variability in vertical mixing, and the strongly temporally varying horizontal salinity gradient.

Snohomish September 2009 in-situ measurements

Bedform and drag

Motivated by the significant asymmetry in drag with respect to tidal phase observed at mooring M1 in September 2008 (*Figure D4*), this past year's analysis of the September 2009 moored ADCP dataset has focused on using single ping beam coordinate velocity data to compute Reynolds stresses and ten minute ensemble averaged velocities at the five mooring sites to determine stress and coefficient of drag as a function of bedform size and roughness. Due to an extreme rain event (100 yr event), zero visibility prevented diver leveling of the mooring platforms and only three (A2, B1, and B3) of the five moorings were sufficiently level to return unbiased Reynolds stress data adequate for evaluating temporal and spatial variability in bed stress.

The spatial variability in C_d is evident (Table D1). Mooring B1 has the smallest drag of the three 2009 moorings, exhibiting a small, yet statistically significant flood-ebb asymmetry. Moorings B3 and A2, on the other hand, exhibit drag coefficients about twice as large as that observed at B1 with no appreciable flood-ebb asymmetry. The influence of bedforms on the measured drag is readily evident when looking at the high resolution multi-beam bathymetry survey data (*Figure D5)*. B1 has much smaller amplitude small-scale bed features in comparison to the other two sites while sites B3 and A2 exhibit similar bed drag for significantly different bedforms: qualitatively, site A2 is rougher over short length scales while B3 exhibits larger scale roughness of slightly larger bedforms relative to A2.

As noted above (see *Figure D4)*, in 2008, we observed strongly asymmetric bed stresses with respect to flood and ebb tide at Mooring M1. Using the high resolution bathymetry measured in 2009[1], an explanation for the asymmetry is readily seen (*Figure D5*, cyan trace). Due to the placement of the mooring M1 in 2008, there is an abrupt transition in bedform shape and roughness upstream and downstream of the mooring. The measured stress for flood is much higher because the cumulative representation of the friction induced by the bedforms preceding the actual measurement site depends on the tidal phase. During flood tide, the mooring measures a cumulatively larger drag due to appreciably rougher bottom over short and moderate (to be quantified below in *Figure D6*) length scales, in comparison to the relative smooth bottom measured for ebb tides.

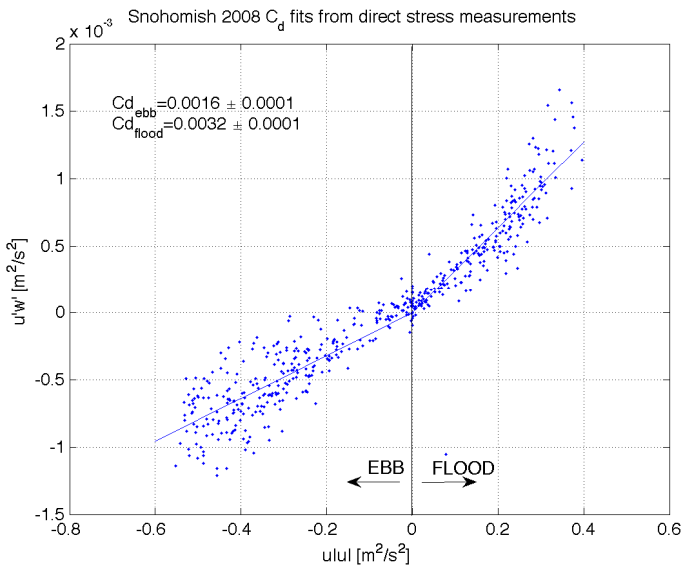

Figure D4. Coefficient of drag 2008 Bottom stress as a function of flow speed squared and C_d for mooring M1.

Table C1. September 2009 Drag Coefficients

Mooring	C_d , Flood	C_d , Ebb
B1	0.0017 ± 0.00004	0.0013 ± 0.00003
B3	0.0036 ± 0.0004	0.0034 ± 0.0003
A2	0.0032 ± 0.0004	0.0026 ± 0.0004

These findings are further clarified for both the 2008 and 2009 data set by looking at power spectral estimates of the bedforms as a function of wavenumber in the along-stream flow direction (*Figure D6*). The flood-ebb asymmetry for M1 is clearly evident in the spectra subdivided between flood and ebb "upstream" bedforms, with significantly larger bedforms being responsible for the larger stresses measured during flood tide for M1.

[1] The 2009 multibeam data for the bedforms surrounding M1 was cross-compared with data from a much coarser survey measured in 2008, and consistency between the two datasets is found to be excellent, in spite of the latter data's significantly lower resolution.

The spectral density of the bathymetry at B1 is nearly two orders of magnitude smaller than the other three moorings shown in *Figure D6*. The differences in scale and amplitude between B3 and A2 are also clear. The peak variance in spectral density for A2 is 35% larger than B3, but is found for length scales twice that for the spectral peak for B3. Yet, as noted above, the differences in scale and bedform amplitude combine to produce a similar overall drag coefficient. The influence of bedform amplitude and length scales on drag coefficient is an area of ongoing interest and research.

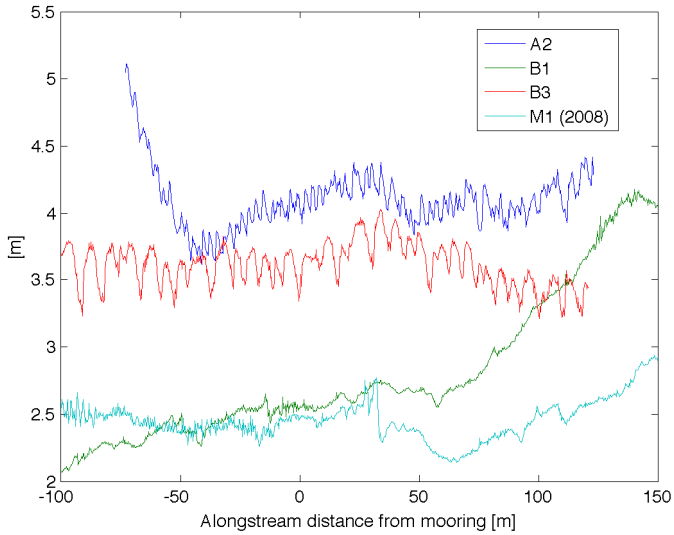

Figure D2. Bedform roughness 2009 Roughness and variability from high resolution multi-beam bathymetry. For each along-stream path, the moorings are located at x=0 m and x increases away from the river mouth.

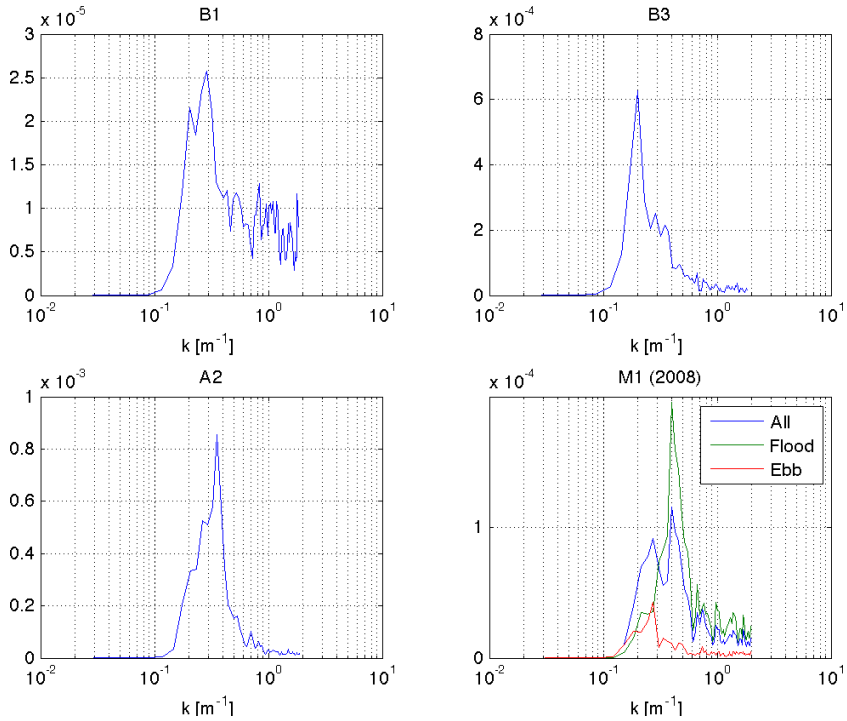

Figure D3. Power spectral density for bedforms Power spectral density of the bedforms from September 2008 (M1) and September 2009 (B1, B3, A2) moorings. Mooring M1 includes separate spectral densities for the flood tide direction (downstream) and the ebb tide direction (upstream).

E: Numerical Modeling

High-resolution SUNTANS simulations

During the past year we have focused on high-resolution simulations in the vicinity of the sill using SUNTANS (Fringer et al., 2006) to determine how the sill at the tip of jetty island influences the surface salinity field. The computational domain for the high-resolution simulations is depicted in Figure E1, which consists of roughly 500,000 horizontal grid cells with resolution varying from 1 m in the vicinity of the sill of interest to 300 m in Possession Sound. Over 70% of the resolution is confined to within 500 m of the sill. The vertical resolution is 0.2 to 0.3 m in the upper 20 m of the water column, and the vertical grid spacing stretches to 30 m in the deepest portion of the domain in the Sound. In total, the three-dimensional domain is discretized with 12 million computational cells, which requires roughly 4 Gb RAM. The bathymetry shown in Figure E2 is what has been resolved by this grid which shows that the sill is reasonably well represented. In the present simulations, the time step size is 0.1 s and is restricted by the horizontal Courant number in the finest cells due to wetting and drying. In this paper we report on the results over a 24-hour tidal cycle during spring (strong) tides. This requires 864,000 time steps, which consumes 48,000 cpu-hours using 200 processors on the MJM machine at the ARL DSRC (3.0 GHz Intel Woodcrest processors).

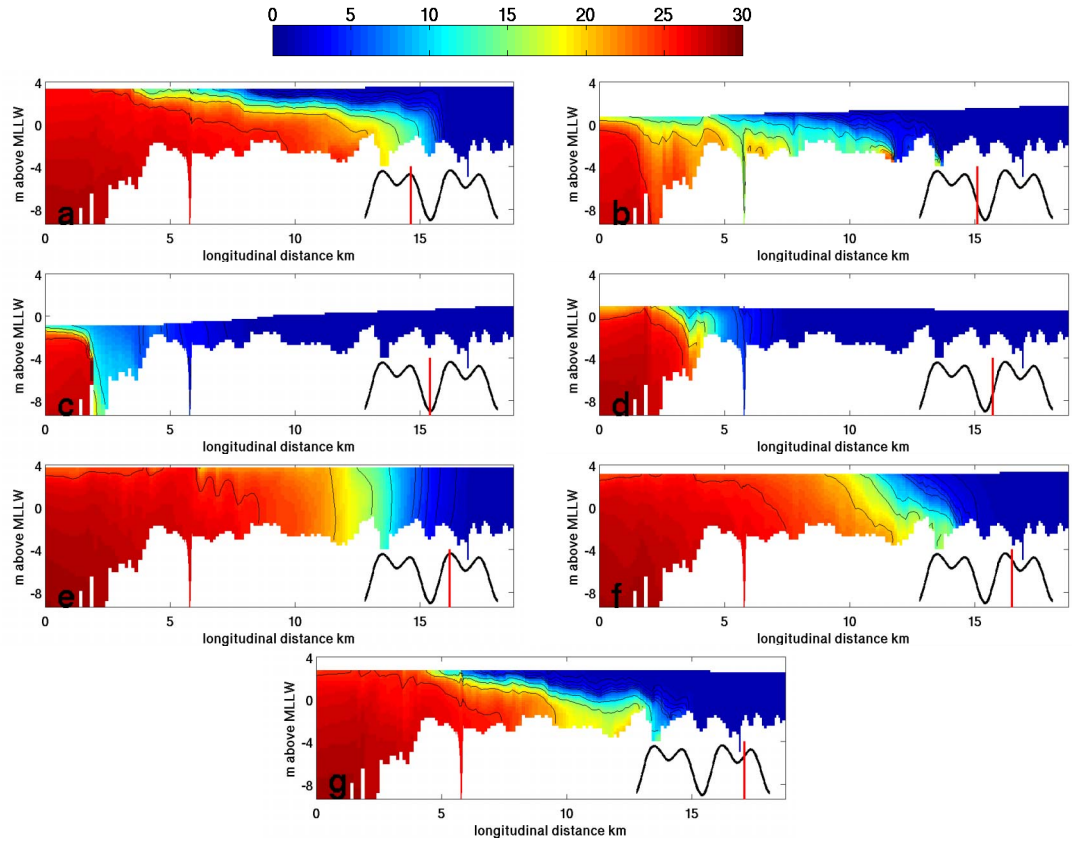

Figure E4: Salinity (in psu) profile along transect E-E' (see Figure E2a) over a tidal cycle. Contours are for every 3 psu. The horizontal axis is the distance along transect from E (left) to E' (right) in km. The tidal stage is shown at the lower-right corner of each panel.

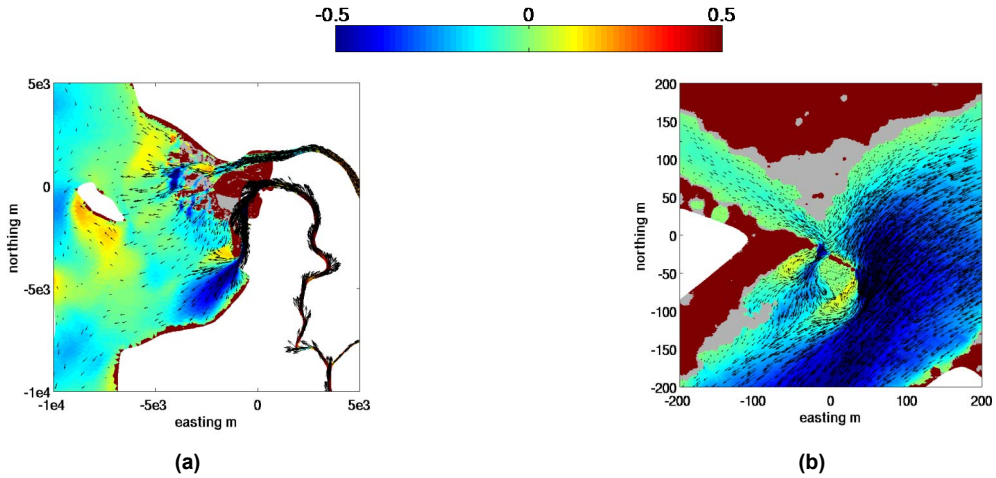

Figure E5: Near-surface velocity field (a) in the estuary and (b) around the sill at low tide. Arrows show the magnitude and direction of the flow and the color indicates the magnitude of the northing velocity (m s^{-1}). Arrows in the two panels are of different scales. Dark red indicates dry areas and gray indicates where the plotted layer is below the local depth.

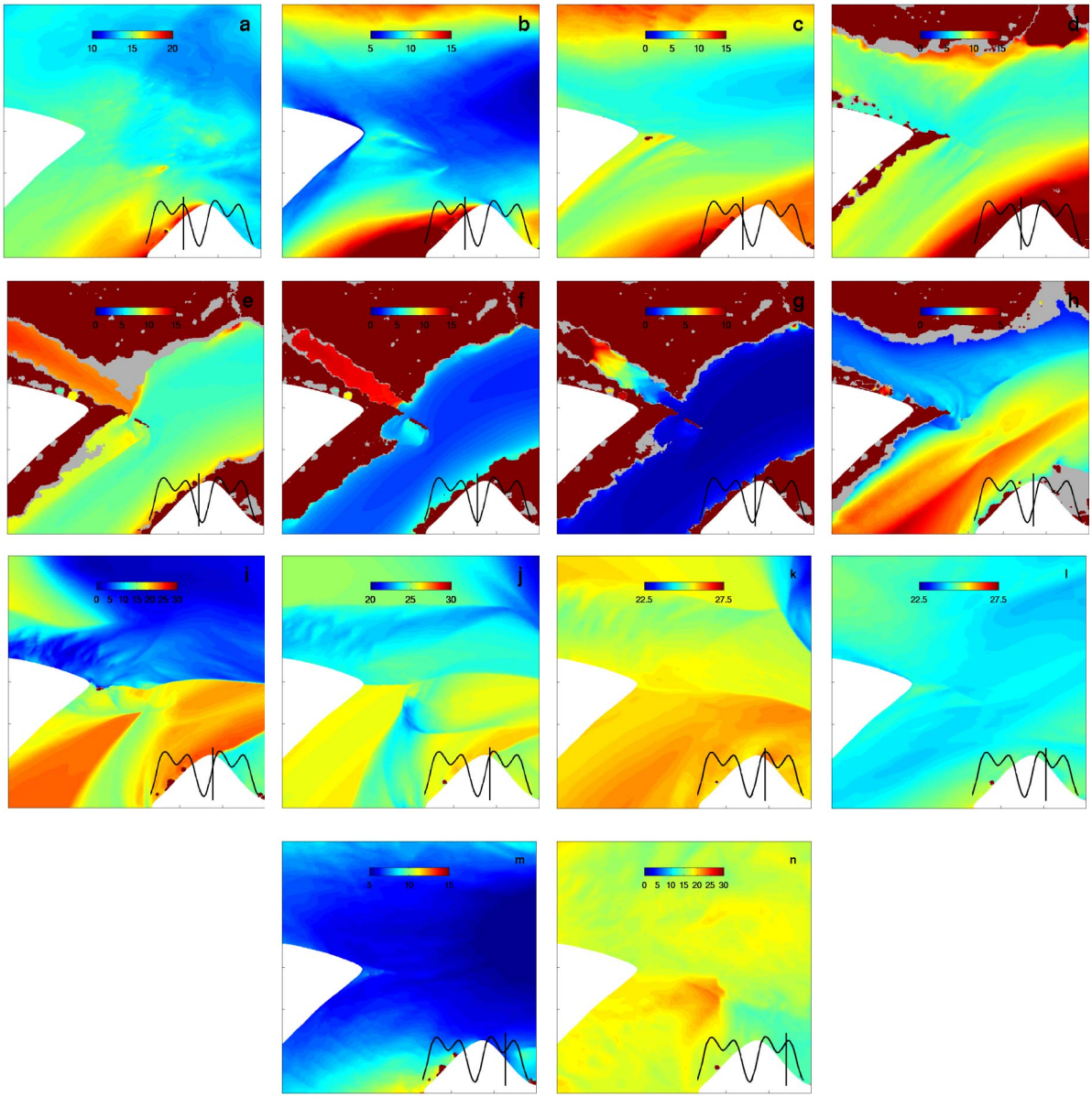

Figure E6: Near-surface salinity distribution (in psu) around the sill in the domain shown in Figure E2(b). Dark red indicates dry areas and gray indicates where the plotted layer is below the local depth. The tidal stage is shown at the lower-right corner of each panel.

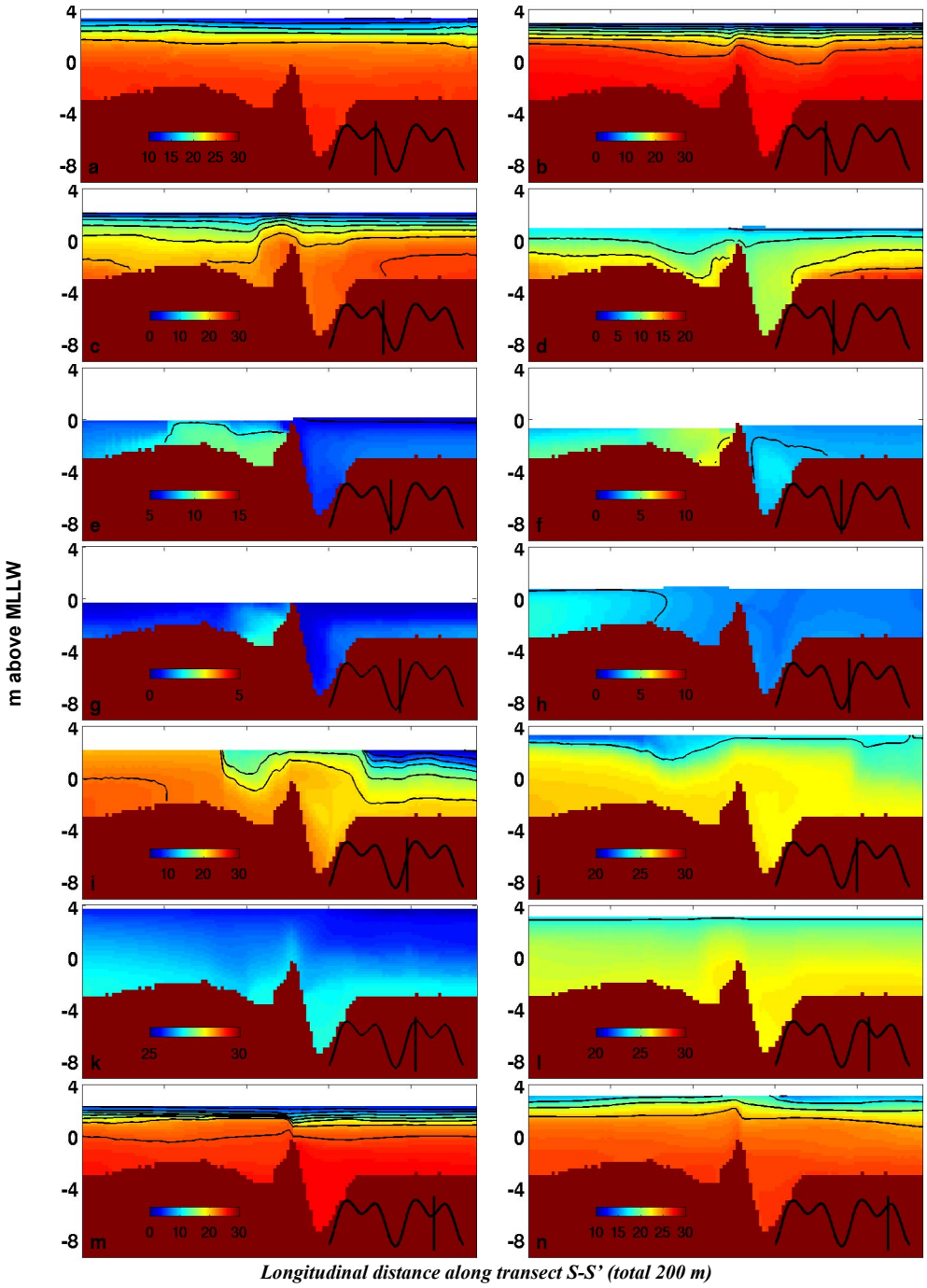

Figure E7: Salinity profile (in psu) along transect S-S' (Figure E2) over a tidal cycle. Contours are for every 3 psu from 3 psu to 27 psu. The horizontal axis is the distance (m) along the transect from S to S'. The tidal stage is shown at the lower-right corner of each panel.

F: Microwave Remote Sensing

We have spent much time this year analyzing the data collected with the bankside radar that was deployed during COHSTREX 2009. The X-band Doppler radar, RiverRad, was deployed in the bed of a pick-up truck beside the Snohomish River during the time that measurements on the APL barge were being made. Data were collected continuously, day and night, from 17:00 PDT on September 9, 2009 to 10:09 PDT on September 25, 2009. The only exceptions were when the radar was being repositioned after the barge had moved. Figure F1 shows the radar in operation with the barge in the background. RiverRad's two antennas were operated with azimuth angles 20° apart. Both were VV polarized. A video camera was aligned with the mean azimuth angle of the antenna and recorded an image of the field viewed by the radar every 30 seconds.

We have derived radial surface velocities from RiverRad for all of the data that were collected. Figure F2 gives an example of a map of radial surface currents produced by the analysis along with data on winds and tides and a map showing the signal-to-noise ratio. While the velocities shown in Figure F2 are radial velocities, in many cases these are oriented nearly along the river axis. We therefore selected sections of some of our images that were near the barge and compared our radar current measurements with those made with a current meter on the barge. The result is shown in Figure F3. The figure shows winds and tides as well as barge currents. The variation of the radar-measured surface currents clearly follows the tidal height in the expected manner. Where comparison with barge currents was possible, the agreement was good. An interesting feature of the radar data was that the Bragg wave phase speed did not need to be added to or subtracted from the first moment of the Doppler spectrum in order to obtain the proper current. This indicated that a significant part of the radar backscatter from the river must have come from objects floating in the river rather than from the rippled surface. This point is driven home in Figure F2 by the fact that large sections of data, including the one compared to barge currents, were taken when the wind speed was nearly zero so that water waves would not have been produced.

We analyzed the entire 2009 data set in the manner shown in Figures F2 and F3 and sent the results to Oregon State University for comparison with the ROMS model run by Tuba Ozkan-Haller. The results of these comparisons for sites north of and near the sharp bend in the river are shown in Figure F4 below. The radial velocities extracted from ROMS agree well with the RiverRad radial velocities in the top row except when RiverRad is looking slightly upwind. These data were taken with the low-azimuth-angle antenna while the rest of the image was formed using data from the high-azimuth-angle antenna. We believe that this indicates a problem with the orientation of the low-azimuth-angle antenna of RiverRad and are looking into the problem. In the bottom row, some discrepancies between radar and ROMS are seen but overall, the transition from high to low radial velocities is in fairly good agreement in the two images.

Figure F1. RiverRad operating on the bank of the Snohomish River with the APL barge in the background. The parabolic antennas are oriented 20° apart in azimuth and the video camera seen above them is pointed at the mean azimuth angle.

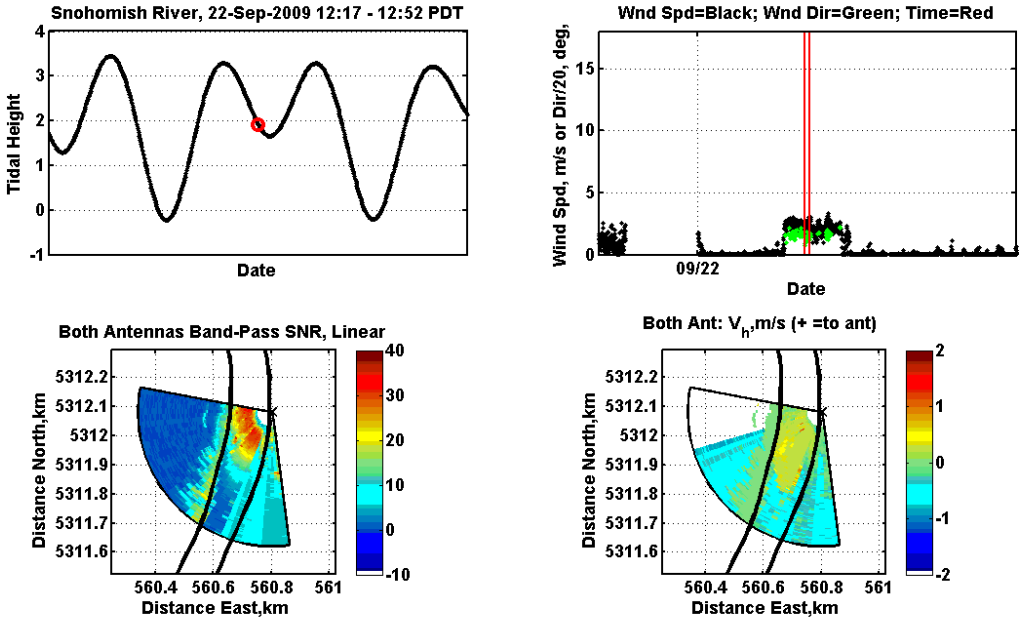

Figure F2. The top left panel shows the time series of river surface height with the red circle showing the time at which two images in the bottom row were taken. The top left panel shows the wind speed and direction versus time with the vertical red lines again indicating the time period when data were collected for the bottom two images. The bottom left image shows RiverRad's signal-to-noise ratio while the bottom right image shows measured radial velocities in m/s. The measurements are only meaningful within the black curves indicating the banks of the Snohomish River. Positive velocities are toward the radar.

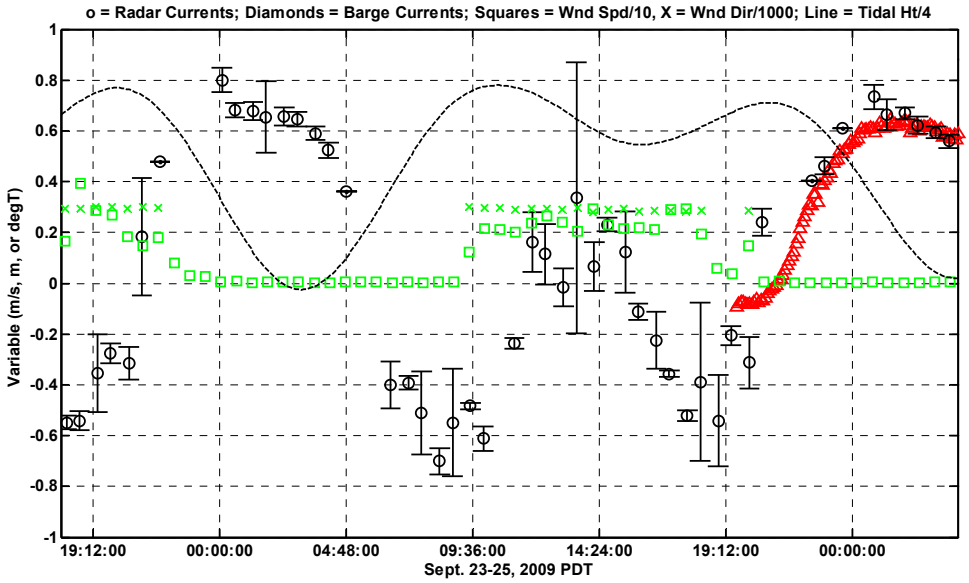

Figure F3. Comparison of currents measured by RiverRad (circles) with tides (dashed line), winds (speed – green squares, direction – green x), and currents measured on the barge with a current meter (red triangles).

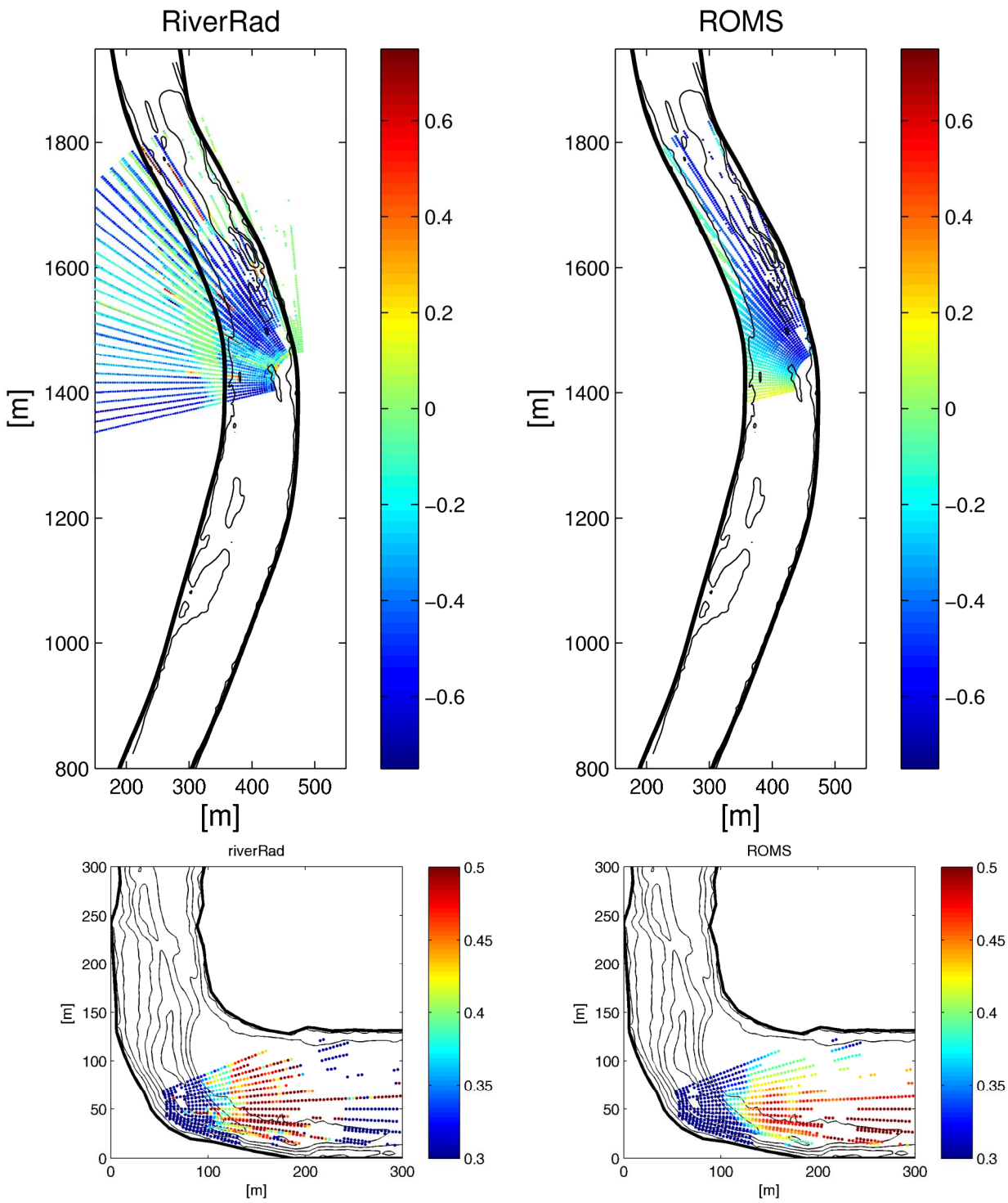

Figure F4. The top row shows radial surface velocities from RiverRad on the left and those extracted from ROMS output on the right. These data were from a site north of the river bend. The bottom row shows the same comparison for data taken just upstream of the river bend. Contours indicate river depth while colors show the velocities in m/s.

IMPACT/APPLICATIONS

Our results demonstrate how currently available prediction schemes and observing systems (remote sensing and AUVs) can be combined for operational applications. Use of IR-based PIV to measure surface turbulence provides a new and powerful tool for area-extensive measurements in the field.

RELATED PROJECTS

Airborne IR/EO measurement system used for the COHSTREX 09 Experiment was developed for Tidal Flats DRI.

REFERENCES

Brumley, B. H. and Jirka, G. H. (1987). Near-surface turbulence in a grid-stirred tank. *Journal of Fluid Mechanics*, 183:235–263.

Kolmogorov, A. N. (1941). The local structure of turbulence in incompressible viscous fluid for very large Reynolds number. *Dokl. Akad. Nauk SSSR 30(4).*

Fringer, O. B., M. Gerritsen, and R. L. Street, 2006, "An unstructured-grid, finite-volume, nonhydrostatic, parallel coastal ocean simulator", *Ocean Modelling*, 14, 139-278.

Nezu, I., Tominaga, A., and Nakagawa, H. (1993). Field measurements of secondary currents in straight rivers. *Journal of Hydraulic Engineering*, 119(5):598–614.

Simpson, J. H., J. Brown, J. Matthews, and G. Allen, 1990, "Tidal straining, density currents, and stirring in the control of estuarine stratification", *Estuaries*, 13, 125-132.

Tamburrino, A. and J. S. Gulliver (1994). Free-surface turbulence measurements in an open channel flow. *ASME, FED,* 181, E. P. Rood and J. Katz, eds., American Society of Mechanical Engineers, New York, p. 103.

Tamburrino, A. and Gulliver, J. S. (2007). Free-surface visualization of streamwise vortices in a channel flow. *Water Resources Research*, 43(W11410).

Wang, B., O. B. Fringer, S. N. Giddings, and D. A. Fong, 2009, "High-resolution simulations of macrotidal estuary using SUNTANS", *Ocean Modelling*, 26, 60-85.

Wang, B., S. N. Giddings, O. B. Fringer, E. S. Gross, D. A. Fong and S. G. Monismith, 2010, "Modeling and understanding turbulent mixing in a macrotidal, salt-wedge estuary", *J. Geophys. Res.,* under review.

PUBLICATIONS

Chickadel, C. C., S. A. Talke, A. R. Horner-Devine, A. T. Jessup, Infrared based measurements of velocity, turbulent kinetic energy, and dissipation at the water surface in a tidal river, *Geosci. Remote Sens. Let.,* 2010 [submitted, refereed].

Giddings, S. N., D. A. Fong, and S. G. Monismith (2010) The role of straining and advection in the intratidal evolution of stratification, vertical mixing, and longitudinal dispersion of a shallow, macrotidal, salt-wedge estuary. J.Geophys. Res. [to appear, refereed].

Giddings, S. N., D. A. Fong, S. G. Monismith, C. C. Chickadel, K. A. Edwards, W. J. Plant, B. Wang, O. B. Fringer, A. R. Horner-Devine, and A. T. Jessup (2010) Frontogenesis and frontal progression of a trapping-generated estuarine convergence front and its influence on mixing and stratification, *Estuaries and Coasts* [submitted, refereed].

Plant, W. J., et al. (2009), Remotely sensed river surface features compared with modeling and in situ measurements, *J. Geophys. Res.-Oceans*, *114*.

Talke, S. A., A. R. Horner-Devine, and C. C. Chickadel (2010), Mixing layer dynamics in separated flow over an estuarine sill with variable stratification, *J. Geophys. Res.-Oceans*, *115*.
Wang, B., S. N. Giddings, O. B. Fringer, E. S. Gross, D. A. Fong and S. G. Monismith. Modeling and understanding turbulent mixing in a macrotidal salt wedge estuary. *J. Geophys. Res*., submitted.